Journal of Oceanology and Limnology
Vol. 44, No. 3, pp. 978-989, 2026
https://doi.org/10.1007/s00343-025-5034-z

Research Paper

A novel simplified and high-precision georeferenced model for multibeam bathymetric data*

Xunpeng YAN[1], Xianhai BU[1, 2, **], Mingzhen XIN[1, 2], Miao FAN[3, 4], Jianxing ZHANG[5], Fanlin YANG[1, 2]

[1] *College of Geodesy and Geomatics, Shandong University of Science and Technology, Qingdao 266590, China*
[2] *Key Laboratory of Ocean Geomatics, Ministry of Natural Resources of China, Qingdao 266590, China*
[3] *School of Marine Science and Technology, Tianjin University, Tianjin 300072, China*
[4] *National Marine Data and Information Service, Tianjin 300171, China*
[5] *Institute of Oceanology, Chinese Academy of Sciences, Qingdao 266000, China*

Received Jan. 27, 2025; accepted in principle Jun. 29, 2025; accepted for publication Aug. 20, 2025

Abstract Multibeam echosounder system (MBES) is an essential acoustic remote sensing technique for seabed topography surveys. The georeferenced model is crucial for the MBES when calculating the bathymetric soundings' geolocation and depth. Existing models are complex and time-consuming, failing to meet the demands of large-scale or real-time data processing. To address these issues, we proposed a simplified and high-precision method. First, two regular sectors with the same vertex are assumed to represent the across-track and along-track beam patterns of the multibeam transmitter and receiver, respectively, instead of two cones in the conventional virtual concentric cone array (VCCA) model. Secondly, the beam vector representing the direction of sound ray tracing is derived by calculating the intersection point coordinates between the two sectors. Finally, an efficient progressive equivalent sound speed profile ray tracing progress is used to obtain the final depth of soundings. Experimental results demonstrate that the proposed method substantially reduces processing time, with reductions of approximately 52% for shallow water data and 84% for deep water data. The root mean square error of depth discrepancies is approximately 0.58% of water depth in overlapping regions of cross-survey lines. Furthermore, the proposed method achieves accuracy comparable to the VCCA algorithm.

Keyword: multibeam echosounder system (MBES); georeferenced model; ray tracing; equivalent sound speed profile

1 INTRODUCTION

The digital bathymetry models (DBMs), which represent seabed topography in digital form, are essential for studying the evolution of the ocean basins, physical oceanographic processes, and benthic habitat analysis (Gula et al., 2015; Ruan et al., 2020; Li et al., 2023; Yu et al., 2024). These models are also critical for a wide range of human activities, including offshore engineering, safe navigation, and underwater archaeology (Ellis et al., 2017; Ogor, 2018; Yang et al., 2020; Janowski et al., 2025). The source data of the DBMs include multibeam echosounder system (MBES), airborne bathymetric LiDAR, airborne photogrammetry, and satellite imagery, particularly in shallow water environments (Janowski et al., 2024). However, multibeam bathymetric data (MBD) serve as a crucial input for compiling high-precision, high-resolution DBMs. For example, the MBD in the latest product GEBCO_2024, a global terrain model for ocean and land, accounts for 15.26% of the total underwater part, and this proportion steadily increased every

* Supported by the National Natural Science Foundation of China (Nos. 42204049, 42206200), the Natural Science Foundation of Shandong Province (No. ZR2022QD008), the Qingdao Natural Science Foundation (No. 24-8-4-zrjj-2-jch), and the National Key Research and Development Program of China (No. 2023YFB3907204)
** Corresponding author: buxianhai2012@163.com

year recently (GEBCO Compilation Group, 2024).

In recent years, the beam number and ping rate of the MBES have steadily increased, exemplified by the R2Sonic 2026 multibeam system, which provides 1 024 soundings per ping and a ping rate of up to 60 Hz (R2Sonic LLC, 2022). This advancement has led to a substantial growth in the volume of data collected during a single survey (Yang et al., 2022). Platforms equipped with MBES are transitioning from traditional survey vessels to autonomous surface vehicles (ASVs) and autonomous underwater vehicles (AUVs) (Sotelo-Torres et al., 2023). These unmanned systems facilitate real-time transmission of MBD to monitor changes in the detected targets and support for simultaneous localization and mapping (SLAM) (Palomer et al., 2016; Norgren and Skjetne, 2018).

The algorithm for calculating the geolocation and depth of each beam by integrating raw multibeam information with various auxiliary sensor data, such as positioning, attitude, and sound velocity, is referred to as georeferenced model. Consequently, the accuracy and efficiency of this model for processing large volumes of soundings significantly affect the representation of real-time topography (Mohammadloo et al., 2020). Within this framework, beam vector calculation and ray-tracing process are among the primary and most time-consuming components.

The calculation of the beam vector is complex due to the influences of various factors, including the transducer’s steering angles (which redirect the main response axis of the beam pattern to different angles for broader coverage), alignment angles, attitudes, and positions (Hughes Clarke, 2003). Consequently, researchers have simplified the beam vector calculation to varying extents. Early studies often equated the receiver’s steering angle of MBES with the beam vector for computational convenience (Hare, 1995). In this approach, the beam incidence angle was calculated in a two-dimensional plane perpendicular to the ship’s heading, which overlooked the effects of the transducer’ alignment angles and attitudes on the beam vector (Hughes Clarke, 2003). To address these issues, Beaudoin et al. (2004) proposed a virtual concentric cone array (VCCA) model, which treats the transmitter and receiver were as two independent units and constructs a virtual array reference frame (ARF) based on the transmitter at the time of sound transmitting and the receiver at the time of sound receiving. Thus, this model rigorously accounts for the steering angles and alignment angles of both the transmitter and receiver, as well as the attitude variations during the sound roundtrip. The VCCA model has also been implemented in the open-source software MB-System. The non-concentric cone array (NCCA) model (Hamilton et al., 2014) further enhances the VCCA by considering the displacement of the transmitter and receiver during the sound roundtrip. However, the NCCA model requires a two-layer iterative process to obtain the beam vector, resulting in longer computation times. To improve efficiency, Bu et al. (2020) developed a simplified NCCA model that combines elements of both VCCA and NCCA, thereby eliminating one iterative process and improving computational efficiency by approximately 17%.

The ray tracing process is executed using a constant-gradient ray tracing algorithm, which traces the sound’s acoustic trajectory in the direction of the beam vector by applying Snell’s law and the sound speed profile (SSP) in the water column. However, this process can be time-consuming and increases with both depth and the sampling density of the SSP (Cartwright et al., 2002; Mohammadloo et al., 2019). To streamline this procedure, Geng and Zielinski (1999) demonstrated that if the integration areas of two SSPs are identical, the resulting ray tracing outcomes are essentially the same. Thus, the intricate multi-layer actual SSP can be substituted with a simple one-layer SSP. The simple SSP is termed the equivalent sound speed profile (ESSP), which significantly reduces the complexity of the ray tracing process, as illustrated in Fig.1. However, since the ESSG is a function of depth, relying on a single ESSP for all beams may result in a loss of accuracy, particularly when the seafloor topography exhibits high variability, as depicted by the two beams in Fig.1 (Xin et al., 2015; Bu et al., 2021). To

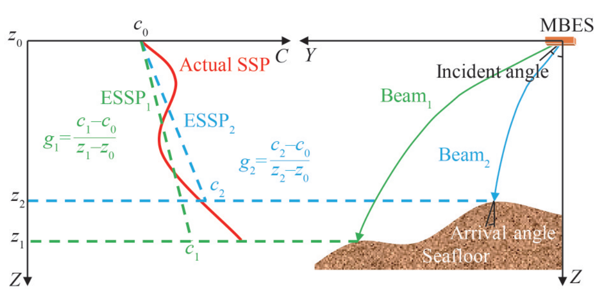

Fig.1 Influence of seafloor topography variation on the calculation of ESSP for different beams

solve this issue, Xin et al. (2015) proposed an iterative ESSP (IESSP) method for accurately calculating the ESSP of each beam in the presence of uneven topography. This approach necessitates multiple iterations, particularly when there is a substantial discrepancy between the depth of the SSP and the seafloor depth.

Consequently, existing georeferenced models offer high accuracy. However, their complexity and time consumption render them unsuitable for rapid, real-time processing of MBD. The primary objectives of this study are to: (1) develop a more efficient and intuitive beam vector calculation method that maintains accuracy while reducing computational complexity; (2) create an enhanced IESSP method to accelerate the calculation speed without sacrificing precision.

To achieve these goals, we proposed a new method that could primarily enhance the beam vector calculation and the ray tracing process, building on the VCCA model and the IESSP method. In the beam vector calculation, two regular sectors with a common vertex are assumed to represent beam patterns of the transmitter and the receiver, rather than the more complex cones used in the VCCA model. Additionally, a progressive ESSP (PESSP) ray tracing method that incorporates initial depths of the soundings from the previous soundings into the IESSP was developed. This enhancement further accelerates the calculation speed of the ESSP for soundings in the subsequent pings. Therefore, the proposed method ensures both accuracy and improved computational efficiency while providing a more intuitive underlying principle.

2 METHOD

2.1 Derivation of the beam vector for MBES

To accurately calculate the beam vector, it is essential to first define the relevant coordinate system. Unlike the VCCA model, which requires constructing of the ARF before transforming to the local level coordinate system (LLCS), the proposed method calculates the beam vector directly within the LLCS. The LLCS is defined as follows: the origin of the coordinate system, O, is located at the midpoint of the line connecting the acoustic center of the transmitter at the time of sound transmission and the acoustic center of receiver at the time of sound reception. The positive direction of the X-axis points to the true north meridian, the positive direction of the Y-axis points to the eastward, and the Z-axis, along with the X and Y axes, form a right-handed orthogonal coordinate system, as shown in Fig.2.

Under ideal conditions, the transmitter unit vector along the X-axis is $\boldsymbol{T}_{\mathrm{X}}=[1,\ 0,\ 0]^T$. The transmitter vector $\boldsymbol{T}_{\mathrm{X}}'$, considering the transmitter's alignment angles ($\omega_{T\mathrm{align}}$, $\varphi_{T\mathrm{align}}$, $\gamma_{T\mathrm{align}}$) and the attitude angles ($\omega_{T\mathrm{att}}$, $\varphi_{T\mathrm{att}}$, $\gamma_{T\mathrm{att}}$) at the time of sound transmission, can be calculated by Eq.1.

$$\boldsymbol{T}_{\mathrm{X}}'=\boldsymbol{R}(\omega_{T\mathrm{att}},\ \varphi_{T\mathrm{att}},\ \gamma_{T\mathrm{att}})\cdot\boldsymbol{R}(\omega_{T\mathrm{align}},\ \varphi_{T\mathrm{align}},\ \gamma_{T\mathrm{align}})\cdot\boldsymbol{T}_{\mathrm{X}}, \quad (1)$$

where $\boldsymbol{R}$ is a three-dimensional rotation matrix with respect to the roll angle φ, pitch angle γ, and yaw angle ω (Beaudoin et al., 2004).

Based on the principles of MBES, it is known that the transmitter sector is perpendicular to the transmitter vector. Therefore, the transmitter vector is the normal vector of the transmitter sector. The normal vector of the transmitter sector, after undergoing a rotation angle, is equivalent to the transmitter vector rotated by the same angle. Thus, the transmitter vector $\boldsymbol{T}_{\mathrm{X}}''$, $\boldsymbol{T}_{\mathrm{X}}'$, after undergoing the transmit steering angle ($\theta_{T\mathrm{steer}}$), can be calculated by Eq.3.

$$\boldsymbol{n}^T_{\mathbf{OZ}}=\boldsymbol{T}_{\mathrm{X}}'\times\mathbf{OZ}, \quad (2)$$

$$\boldsymbol{T}_{\mathrm{X}}''=\boldsymbol{R}(\theta_{T\mathrm{steer}})\boldsymbol{T}_{\mathrm{X}}', \quad (3)$$

where $\boldsymbol{n}^T_{\mathbf{OZ}}$ is the rotation axis for the transmitter vector; $\boldsymbol{R}(\theta_{T\mathrm{steer}})$ is the rotation matrix of the $\boldsymbol{n}^T_{\mathbf{OZ}}$; $\mathbf{OZ}$ is the Z-axis, $\mathbf{OZ}$=[0,0,1].

Similarly, the receiver vector $\boldsymbol{R}_{\mathrm{X}}''$ can be calculated by the receiver's alignment angles ($\omega_{R\mathrm{align}}$, $\varphi_{R\mathrm{align}}$, $\gamma_{R\mathrm{align}}$), the attitude angles ($\omega_{R\mathrm{att}}$, $\varphi_{R\mathrm{att}}$, $\gamma_{R\mathrm{att}}$) and receive steering angle $\theta_{R\mathrm{steer}}$ at the time of sound reception.

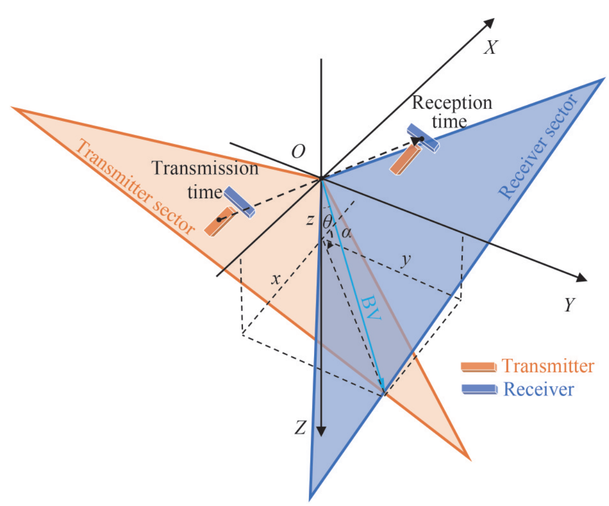

Fig.2 Illustrative schematic of the beam vector

According to geometric principles, the direction vector of the line of intersection between two planes can be given by the cross product of their normal vectors. Therefore, the beam vector **BV**=[x, y, z], the intersection line between the transmitter sector and the receiver sector, can be obtained by taking the cross product of the normal vector of the transmitter sector and the normal vector of the receiver sector:

$$\mathbf{BV}=\boldsymbol{T}_{\mathrm{X}}''\times\boldsymbol{R}_{\mathrm{X}}''. \tag{4}$$

Thus, the beam incidence angle θ and azimuth angle α of the beam vector can be calculated as:

$$\begin{cases}\theta=\tan^{-1}(z/\sqrt{x^2+y^2})\\ \alpha=\tan^{-1}(x/y)\end{cases}. \tag{5}$$

The VCCA model typically requires 16 equations to calculate the beam vector (Beaudoin et al., 2004). In contrast, the proposed method in this paper requires only 8 equations (the calculation of $\boldsymbol{R}_{\mathrm{X}}''$, like that of $\boldsymbol{T}_{\mathrm{X}}''$, also needs 3 equations). Most of these formulas involve matrix operations, which significantly simplify the computational process.

2.2 Progressive ESSP ray tracing progress

As shown in Fig.3, the principle of the PESSP involves using the estimated depth z_e from the previous soundings to replace the maximum depth $z_{\max}$ of the SSP as the initial depth in IESSP. The key to the PESSP is the accurate estimation of the z_e, which is the closest to the actual depth of P.

The calculation steps of the PESSP are as follows:

I. Previous sounding set search: the previous sounding set is represented by $\boldsymbol{P}_{i,j}=\{p_{i,j}: i, j\in[-n, 0]\}$, where i is the ping number and j is the beam number, n is the search range. When n=2, it corresponds to selecting the previous 8 soundings, as shown in Fig.4.

II. Outlier removal of preceding sounding set: Due to the influence of complex underwater environment and measurement characteristics, there may be some outliers in MBD. These outliers can be filtered out using the statistical outlier removal method (Breunig et al., 2000).

III. Initial depth calculation: The initial depth z_e can be calculated using the inverse distance interpolation method.

$$z_e=\sum\nolimits_{i=-n}^{0}\sum\nolimits_{j=-n}^{0}\frac{z_{i,j}}{d_{i,j}^2}\Big/\sum\nolimits_{i=-n}^{0}\sum\nolimits_{j=-n}^{0}\frac{1}{d_{i,j}^2}, \tag{6}$$

where $d_{i,j}$ is the planar distance from $p_{i,j}$ to P. However, the planar position of P is unknown before georeferenced model. But the planar position of P can be inferred based on the assumption of constant vessel speed over a small range and equal spacing between beams in the adjacent pings.

IV. Iterative calculation: The integral area S_e of the actual SSP relative to the zero-gradient SSP in the range of [z_0, z_e], the ESSG (g_e) and the ray arrival angle (θ_e) at the seafloor, can be computed by Eq.7.

$$\begin{cases}S_e=\sum S_i\\ g_e=2S_e/(z_e-z_0)^2\\ \theta_e=2\arctan(\mathrm{e}^{tg_e})\end{cases}, \tag{7}$$

where S_i is the integral area of the actual SSP relative to the zero-gradient SSP in the i^{th} water layer; z_0 is the depth of the transducer; t is the travel time. Then, the depth z and across distance y corresponding to θ_e can be calculated by Eq.8.

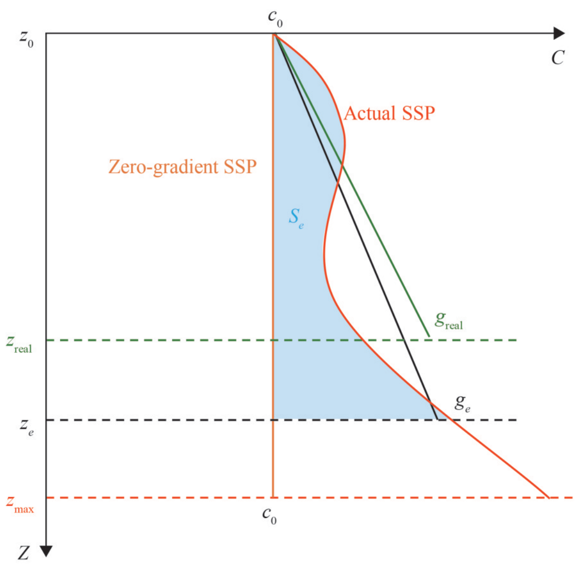

Fig.3 Illustrative schematic of the PESSP

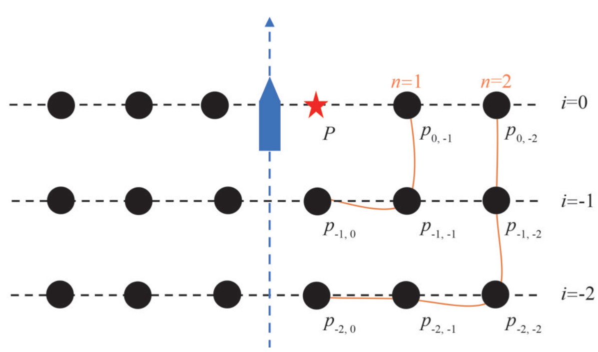

Fig.4 Illustrative schematic of the previous sounding set

$$\begin{cases} z = R(\sin\theta_e - \sin\theta) \\ y = R(\cos\theta - \cos\theta_e) \end{cases}, \tag{8}$$

where R is the radius of the sound ray propagation arc, R=1/ρg; ρ is the Snell constant; θ is the beam incidence angle, which can be calculated using Eq.5.

V. Result output: Determine if the set precision ε is satisfied, i.e., if $(z-z_e)\leq\varepsilon$ is satisfied, terminate the iteration and output the depth z and across distance y; otherwise, perform z_e=z and repeat step (IV) until the set precision is satisfied.

It is important to note that for the first soundings in the MBES swath, as there are no previous soundings, the maximum depth from the SSP can be used as the initial depth. Otherwise, the previous soundings are only searched within the first ping for the first ping soundings.

3 EXPERIMENT

To validate the effectiveness of the proposed method, two cross-lines of MBES data were selected from both shallow-water and deep-water datasets, as shown in Fig.5. The shallow-water data were collected using a Kongsberg EM2040 system in Wellington Harbor, New Zealand, with a depth range of 11–21 m. The number of pings for Line 1 and Line 2 are 1 582 and 1 272, respectively, with each ping consisting of 400 beams. The coordinates of the shallow-water data depicted in the Fig.5a are based on the Universal Transverse Mercator (UTM) projection, specifically using Zone 60S. The deep-water data were obtained using a Kongsberg EM302 system in the northwestern Gulf of Mexico during cruise EX1402L2, covering a depth range of 849–1 381 m. The number of pings for Line 3 and Line 4 are 2 782 and 2 110, respectively, with each ping consisting of 432 beams. The coordinates of the deep-water data depicted in the Fig.5b are based on the UTM projection, specifically using Zone 15N. Additional properties of the two MBESs surveys are shown in Table 1. Furthermore, the two MBESs incorporate multi-sector feature to realize real-time motion compensation, with the beam steer angles smaller at central sector and larger at outer sectors of the multibeam swath.

During the experimental process, the two datasets were also processed by the VCCA model and the constant-gradient ray tracing algorithm. The results served as a reference for comparison with our method. The depth bias in the overlapping area of the cross lines was calculated to assess the consistency of our method at the same area. Statistical analyses of the depth and horizontal differences between our method and the reference results were conducted to verify the accuracy of our approach.

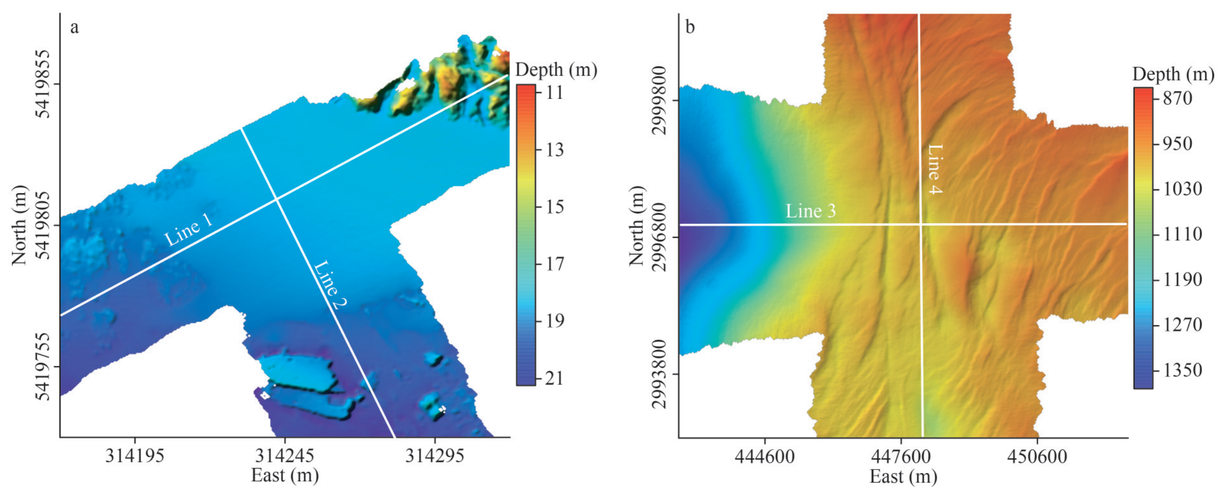

Fig.5 Seafloor topographic maps of the experimental data with cross lines

a. shallow-water data; b. deep-water data.

Table 1 Properties of the two MBESs surveys

Dataset	MBES	Frequency (kHz)	Pulse length	Beam width	Ping rate (Hz)	Swath width (°)
Shallow-water	EM 2040	300	324 µs CW to 6 ms FM	1°×1°	20	120
Deep-water	EM 302	30	0.4 ms CW to 200 ms FM	0.5°×1°	<1	120

3.1 Analysis of depth biases in the overlapping area

To calculate the depth bias in the overlapping area of the cross-track lines, one of the survey lines serves as reference line whereas another line serves as check line. Pairs of tie points from the same location are searched in a given neighbor area and are calculated by inverse distance weighting interpolation algorithm. Thus, there are 6 568 tie points in the shallow-water data and 34 844 tie points in the deep-water data. The depth bias for these tie points is computed and statistically analyzed, as shown in Table 2. The distribution histogram and spatial distribution are presented in Fig.6.

As shown in Table 2, for both shallow-water and deep-water datasets, the mean absolute error (MAE), root mean square error (RMSE), the maximum and minimum of the depth biases in the overlapping area of cross-track lines are generally consistent between the VCCA and our method. The RMSE for the shallow-water and the deep-water datasets is 0.58% and 0.28% of water depth, respectively. Furthermore, there are no soundings exceeding the limit of the International Hydrographic Organization (IHO) S-44 (Edition 6.1.0) special order (IHO, 2022).

Table 2 Statistics of the depth bias in the overlapping area of cross-lines

Dataset	Method	Range (m)	MAE (m)	RMSE (m)
Shallow-water	VCCA	-0.27–0.28	0.08	0.10
	Our method	-0.27–0.26	0.08	0.10
Deep-water	VCCA	-8.73–8.42	1.92	2.40
	Our method	-8.60–8.81	2.01	2.52

As shown in Fig.6, the histograms and spatial distribution of depth biases in the overlapping area of the cross-track lines are also generally consistent between the VCCA and our method. Thus, the results of our method are similar both shallow-water and deep-water datasets. This indicates that the results obtained from our method align closely with those of the VCCA. Furthermore, the depth bias in the central area of the cross-track lines is smaller than that in the outer area (Fig.6b–c & e–f). In the deep-water dataset, the spatial distribution of depth bias is influenced by the seafloor topography (Fig.6e & f), as the footprint of the soundings covers a larger area (approximately 800 m^2 in the experimental data), resulting in higher bathymetric uncertainty.

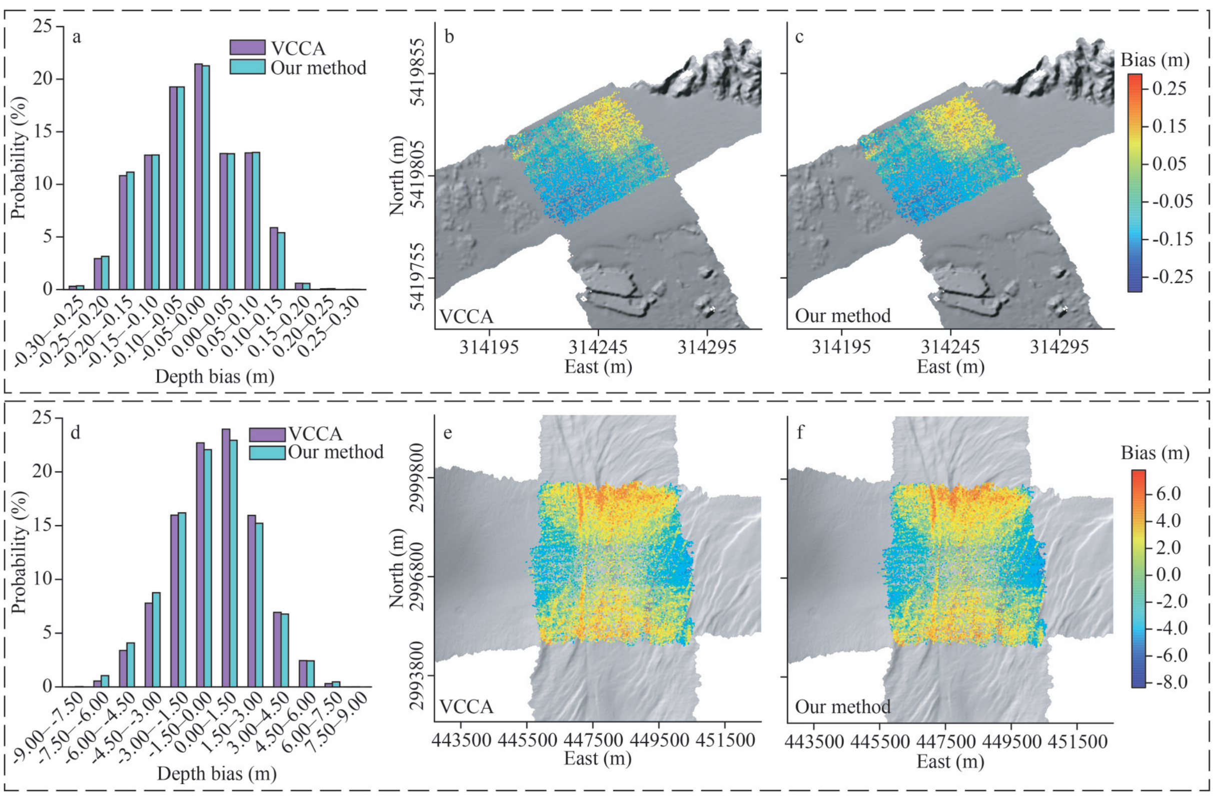

Fig.6 Histograms of depth bias in the shallow-water (a) and deep-water (d) datasets; spatial distribution of depth bias calculated by the VCCA (b) and our method (c) in the shallow-water dataset; spatial distribution of depth bias calculated by the VCCA (e) and our method (f) in the deep-water dataset

3.2 Statistical analysis of the depth and horizontal differences

Data from Line 1 in the shallow-water and Line 3 in the deep-water datasets were utilized to statistically analyze the depth and horizontal differences between our method and the VCCA. The statistical results are presented in Table 3, while the distribution histograms can be seen in Fig.7d & h. Additionally, the relationship between horizontal difference, depth difference and beam incidence angle in single ping is illustrated in Fig.7c & g.

As shown in Table 3, in the shallow-water area, the maximum depth difference for the same beam between our method and the VCCA is 0.06 m, with the MAE and RMSE both being less than 0.005 m. The average depth difference is within 0.01% water depth (%*Z*). In the deep-water area, the maximum depth difference is 0.57 m, with the MAE and RMSE both being less than 0.1 m. The average depth difference is within 0.009% water depth.

As shown in Fig.7a–c & e–g, both horizontal and depth differences increase with the beam incidence angle in the two experimental survey lines. In shallow-water data, the depth difference remains relatively small. In deep-water area, the depth difference is also minimal when the beam incidence angle is less than 50°. Because the edge beams have a larger steering angle compared to the nadir beam, it results in weaker echo signal strength and a longer propagation path in the water, ultimately leading to greater uncertainty in depth measurement. However, when the incidence angle exceeds 50°, the depth difference increases rapidly. The horizontal difference in shallow-water data can be categorized into three segments (S1–S3 in Fig.7c), whereas in the deep-water data, it can be divided into eight segments (S1–S8 in Fig.7g). This segmentation corresponds to the number of multibeam transmitted sectors in the multibeam system, as different transmitted steering angles are employed for each sector.

In Fig.7d & h, it is evident that the depths calculated by our method is generally deeper than those obtained by the VCCA. However, the depth differences are predominantly concentrated near zero. Specifically, in the shallow-water data, approximately 95% of the depth differences are less than 0.01 m, whereas in the deep-water data, about 91% of the differences are less than 0.2 m.

Table 3 Statistical of depth difference within the same beam

Dataset	Range (m)	MAE (m)	RMSE (m)	%*Z*
Shallow-water	0.00–0.06	0.002	0.004	0.010
Deep-water	-0.10–0.57	0.04	0.09	0.009

3.3 Efficiency comparison

As shown in Table 4, our method significantly reduces the total computation time for the beam vector and ray tracing processes compared to the VCCA, achieving reductions of approximately 52.29% in shallow-water dataset and 83.64% in deep-water dataset. In both shallow-water and deep-water datasets, the computation time for the beam vector is decreased by over 45%. Specifically, the computation time for the ray tracing process is reduced by about 58% in shallow-water dataset and 91% in deep-water dataset, with the most substantial reduction observed in the deep-water dataset. This greater reduction in deep-water dataset is attributable to the increased number of SSP layers that typically correspond to greater water depths, which results in a higher computational load for the constant gradient ray tracing algorithm.

The average computation time per ping for the shallow-water and deep-water datasets using our method is 9.5 and 11.9 ms, respectively, both of which are less than the minimum travel time of 13.4 ms for the shallow-water dataset. However, the average computation time per ping for the shallow-water and deep-water datasets using VCCA is 19.9 and 72.7 ms, respectively, both of which are only less than the minimum travel time of 1.19 s for the deep-water dataset. Thereby, our method meets the real-time georeferencing requirements for ASV and AUV surveys.

4 DISCUSSION

4.1 Analysis of the impact of SSP layer count and water depth on computation time

To analyze the impact of SSP layer count and water depth on the computation time, the computation time of each sounding and the SSP layer count were recorded in both the shallow-water and deep-water datasets. Additionally, under the condition that the SSP integral area remained unchanged, the SSP for the deep-water dataset was interpolated to double the number of layers. This was done to analyze the computation time for SSP with different sampling densities at the same water depth. The results are presented in Table 5.

As shown in Table 5, the computation time of the beam vector module in our method in three cases is

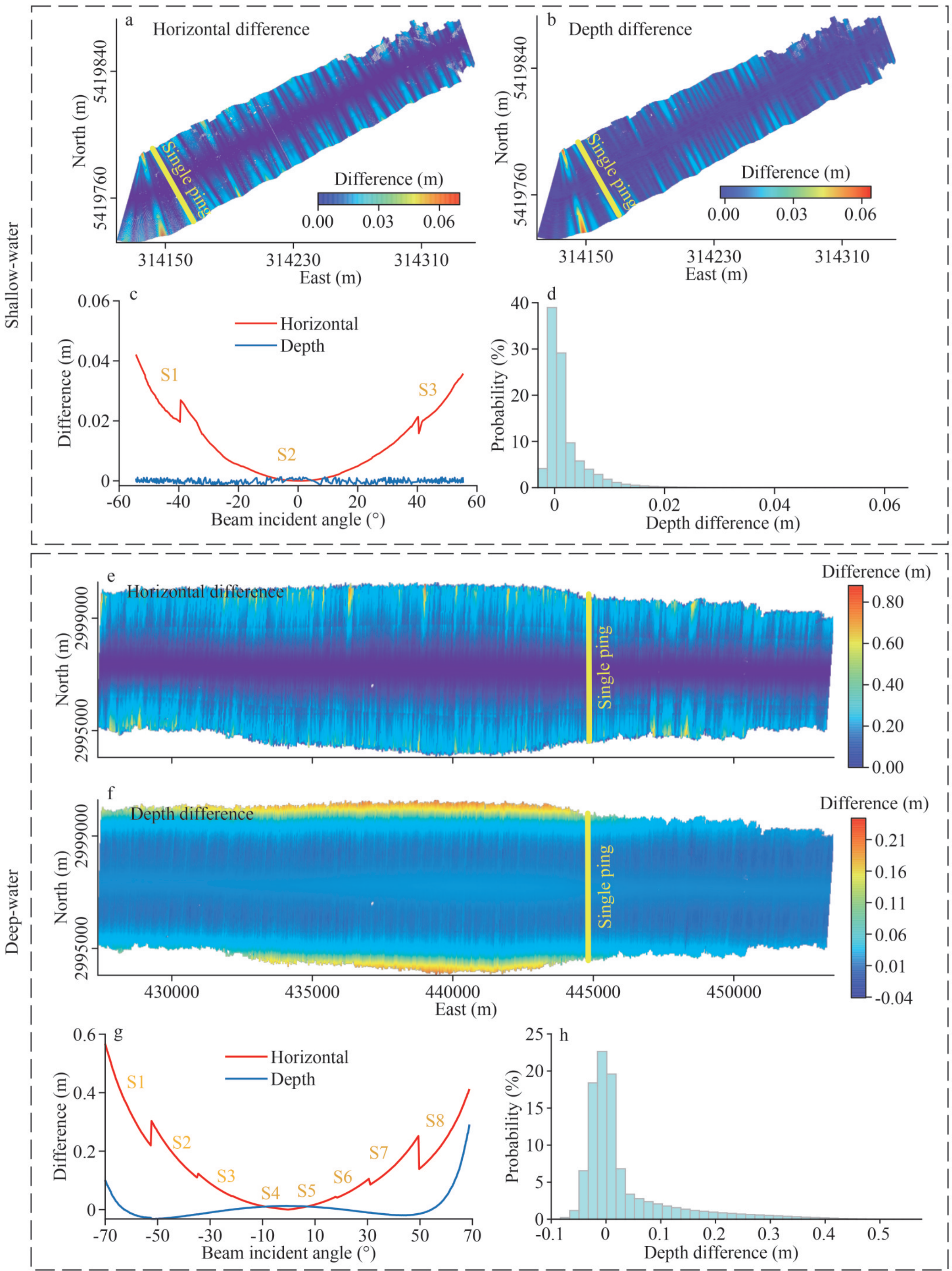

Fig.7 Spatial distribution of horizontal (a) and depth (b) difference, single ping (c) and histograms of depth (d) difference between our method and the VCCA in the shallow-water datasets; spatial distribution of horizontal (e) and depth (f) difference, single ping (g) and histograms of depth (h) difference between our method and the VCCA in the deep-water datasets

S1–S3 in (c) and S1–S8 in (g) represent the MBES of multiple sectors.

13.3, 13.2, and 13.3 ns, with the maximum and minimum values differing by only 0.8%. So, the computation time of the beam vector module in our method is independent of both water depth and the SSP layer count. This is because the beam vector calculation is only dependent on the transducer alignment angle and attitude angle. Additionally, the constant-gradient ray tracing algorithm is positively correlated to the SSP layer count. In contrast, the computation time for PESSP is independent of the

Table 4 Time-consuming for our method and the VCCA

Method	Dataset	Module	Time consuming (s)	Time saving (%)
VCCA	Shallow-water	Beam vector	16.08	No data
		Ray tracing	15.34	
		Total	31.42	
	Deep-water	Beam vector	34.37	
		Ray tracing	167.89	
		Total	202.26	
Our method	Shallow-water	Beam vector	8.54	46.89
		Ray tracing	6.45	57.95
		Total	14.99	52.29
	Deep-water	Beam vector	18.86	45.12
		Ray tracing	15.22	90.93
		Total	33.08	83.64

Table 5 Time-consuming for beam vector and ray tracing of each sounding

Dataset	SSP layer count	Module	Time-consuming (ns)
Shallow-water	58	Beam vector	13.3
		Constant-gradient ray tracing	24.1
		PESSP	10.3
Deep-water	258	Beam vector	13.2
		Constant-gradient ray tracing	139.6
		PESSP	12.5
	516	Beam vector	13.3
		Constant-gradient ray tracing	280.3
		PESSP	12.8

SSP layer count, as PESSP uses an ESSP with a single water layer for ray tracing. Therefore, the computational efficiency advantage of our method becomes more significant as the number of SSP sampling layers increases, especially in deeper waters.

4.2 The advantage of PESSP compared to IESSP

The PESSP was developed to reduce the number of iterations required in IESSP calculations. To illustrate the advantages of PESSP compared to IESSP, the deep-water dataset was used as an example. The IESSP required approximately 7 iterations per sounding to converge and obtain accurate depth, while the PESSP only required 3 iterations. As a result, the computation time of the PESSP is only 42.9% of that of the IESSP, demonstrating a significant improvement in efficiency.

In Section 2.2, we discuss the use of statistical methods to filter out outliers and acknowledge that these methods are generally effective in most cases. However, when the overall quality of the MBD is suboptimal, the removal of outliers may occasionally fail. To evaluate the robustness of the PESSP method, we used the deep-water dataset for experiments, assuming the initial depth was half of the true depth to simulate the influence of outliers. The results demonstrate that the PESSP method still requires only 4 iterations to accurately determine the depth, confirming its robustness.

4.3 Limitation

The method proposed in this paper incorporates two simplifications in the calculation of the beam vector: 1) the displacement, which consists of the static offset and the dynamic offset resulting from vessel movement during the sound roundtrip between the transmitter and the receiver, is neglected. Thus, three-dimensional errors caused by this displacement were introduced in the experimental datasets (Hamilton et al., 2014), contributing to depth biases in overlapping area (Fig.6); 2) in the presence of the steering angle, the multibeam transmitted and received beam patterns form a conical surface (Hamilton et al., 2014), with their intersection with the seafloor forming two hyperbolas. The proposed method simplifies the transmitted and received beam patterns into two three-dimensional sectors (Fig.2), thereby introducing an approximation error, as illustrated in Fig.8.

The NCCA accounts for these factors, making it closer to the real sound propagating scenario and achieving higher computational accuracy. However, it requires iterative solving when calculating beam vector and water depth, leading to slower computation speeds (Bu et al., 2020).

To evaluate the effect of the displacement in the experimental datasets, the deep-water data (Line 3) was also processed by the NCCA model. The horizontal and depth differences between the results of our method and the NCCA were compared, as shown in Fig.9.

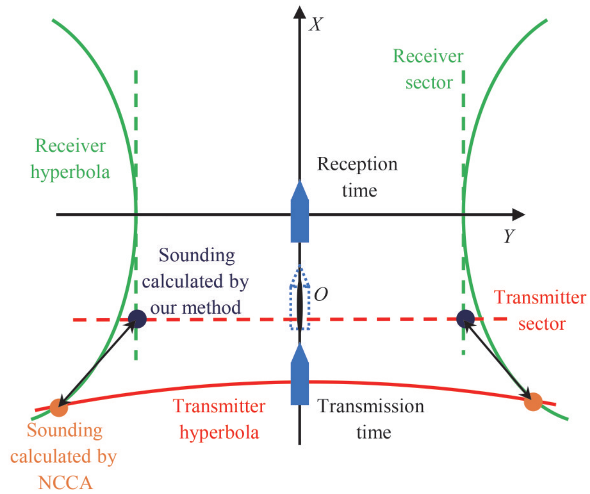

Fig.8 Combined effect of transducer displacement and steering angles on the multibeam footprints

As shown in Fig.9a–c, the horizontal and depth differences increase with the beam incidence angle.

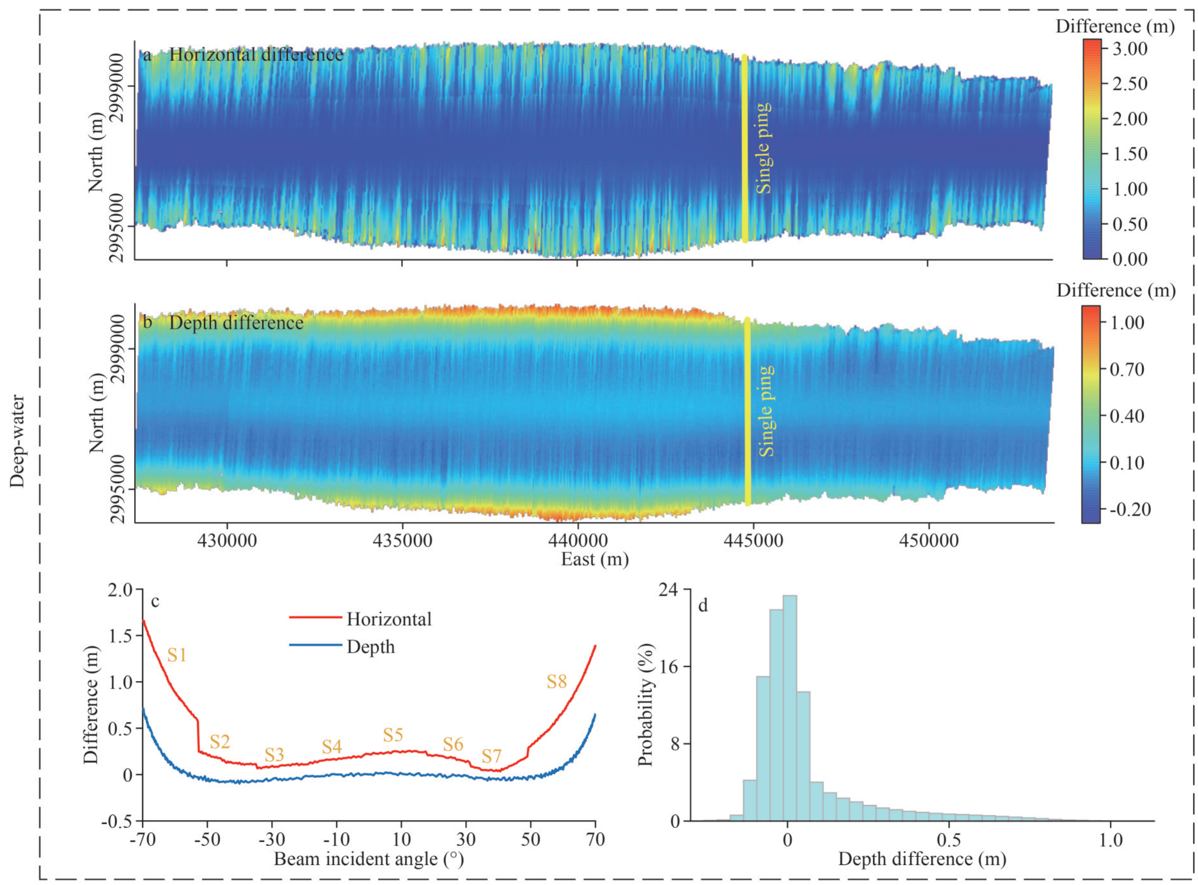

Fig.9 Spatial distribution of horizontal (a) and depth (b) difference, single ping (c) and histograms of depth difference (d) between our method and the NCCA in the deep-water dataset Line 3

When the beam incidence angle is less than 50°, the differences remain relatively small (less than 0.5 m); however, once the angle exceeds 50°, the differences increase rapidly (Fig.9c). Therefore, in the deep-water data, the approximation error can be minimized by reducing the receiver's steer angle. Furthermore, the horizontal difference still exhibits a strong correlation with the multibeam transmission sector (S1–S8 in Fig.9c). The depth differences between our method and the NCCA are primarily concentrated around 0, with the maximum depth difference being less than 1.2 m (Fig.9d). Compared to the water depth, these differences can be considered negligible.

By comparing Figs.8 & 9, it is evident that the difference between our method and the NCCA are greater than those between our method and the VCCA, as both the VCCA and our method disregard the displacement. However, the georeferencing time required by NCCA was 1 293.64 s, whereas our method reduced this time by approximately 97.4%.

Therefore, to overcome the current limitations of our method, future research should prioritize two critical improvements to enhance accuracy. First, in our current method, the coordinate origin is set at the midpoint of the line connecting the acoustic center of the transmitter at the time of sound transmission and the acoustic center of receiver at the time of sound reception. In subsequent refinements, different coordinate origins could be adopted for the acoustic center of the transmitter and receiver. This adjustment would help eliminate static offset errors and dynamic offset errors induced by vessel motion between transducers. Second, multiple sectors could be employed to better approximate the conical surfaces of the transmitting and receiving beam patterns. By doing so, the intersections of these multiple sectors with the seafloor would form polyline approximations, allowing for a closer fit to the hyperbolas in the NCCA. These two improvements are expected to enhance the computational accuracy of the georeferenced model while maintaining computational efficiency.

5 CONCLUSION

To enhance the computational efficiency of the georeferenced model for the MBES while maintaining accuracy, we developed a novel method that could primarily improve the beam vector calculation and ray tracing processes. The proposed method simplifies the VCCA model and improves the IESSP method. Beam vectors are calculated directly by multiplying several matrices, offering a more intuitive and convenient solution. In the ray tracing process, a progressive ESSP technique is employed to reduce the number of iterations required for calculating the ESSP for extensive soundings. The effectiveness of the proposed method in terms of both accuracy and efficiency has been validated using multibeam datasets with cross-track lines from both shallow and deep water. The new model meets the IHO S-44 (Edition 6.1.0) special order standards and significantly enhances computational speed by over 52%, providing a valuable reference for the rapid real-time processing of extensive soundings acquired by unmanned platforms.

6 DATA AVAILABILITY STATEMENT

The datasets generated during and/or analyzed during the current study are available from the corresponding author on reasonable request.

7 ACKNOWLEDGMENT

We thank NOAA (Geospatial Data and Services of the National Oceanic and Atmosphere Administration) and the BGS (British Geological Survey) for providing the data.

References

Beaudoin J D, Hughes C J E, Bartlett J E. 2004. Retracing (and re-raytracing) Amundsen's journey through the northwest passage. *In*: Canadian Hydrographic Conference.

Breunig M M, Kriegel H P, Ng R T et al. 2000. LOF: identifying density-based local outliers. *In*: Proceedings of the 2000 ACM SIGMOD International Conference on Management of Data. ACM, Dallas, Texas, USA. p.93-104, https://doi.org/10.1145/342009.335388.

Bu X H, Yang F L, Ma Y et al. 2020. Simplified calibration method for multibeam footprint displacements due to non-concentric arrays. *Ocean Engineering*, **197**: 106862, https://doi.org/10.1016/j.oceaneng.2019.106862.

Bu X H, Yang F L, Xin M Z et al. 2021. Improved calibration method for refraction errors in multibeam bathymetries with a wider range of water depths. *Applied Ocean Research*, **114**: 102778, https://doi.org/10.1016/j.apor.2021.102778.

Cartwright D S, Hughes-Clarke J E. 2002. Multibeam surveys on the Frazer River delta, coping with an extreme refraction environment. *In*: Proceedings of Canadian Hydrographic Conference. Montreal, Canada. p.1-23.

Ellis J I, Clark M R, Rouse H L et al. 2017. Environmental management frameworks for offshore mining: the New Zealand approach. *Marine Policy*, **84**: 178-192, https://doi.org/10.1016/j.marpol.2017.07.004.

GEBCO Compilation Group. 2024. GEBCO_2024 Grid. Retrieved December 7, 2024, from https://www.bodc.ac.uk/data/published_data_library/catalogue/10.5285/1c44ce99-0a0d-5f4f-e063-7086abc0ea0f/.

Geng X Y, Zielinski A. 1999. Precise multibeam acoustic bathymetry. *Marine Geodesy*, **22**(3): 157-167, https://doi.org/10.1080/014904199273434.

Gula J, Molemaker M J, McWilliams J C. 2015. Gulf stream dynamics along the Southeastern U. S. Seaboard. *Journal of Physical Oceanography*, **45**(3): 690-715, https://doi.org/10.1175/jpo-d-14-0154.1.

Hamilton T, Beaudoin J D, Hughes C J E. 2014. A more precise algorithm to account for non-concentric multibeam array geometry. *In*: Canadian Hydrographic Conference.

Hare R. 1995. Depth and position error budgets for multibeam echosounding. *International Hydrographic Review*, **72**(2): 37-69.

Hughes Clarke J E. 2003. Dynamic motion residuals in swath sonar data: Ironing out the Creases. *The International Hydrographic Review*, **4**(1): 6-23.

International Hydrographic Organization. 2022. IHO Standards for Hydrographic Surveys, Edition 6.1.0. Monaco. International Hydrographic Organization, Monaco, https://doi.org/10.25607/OBP-1354.3.

Janowski Ł, Pydyn A, Popek M et al. 2025. Towards better differentiation of archaeological objects based on geomorphometric features of a digital elevation model, the case of the Old Oder Canal. *Archaeological Prospection*, **32**(1): 47-58, https://doi.org/10.1002/arp.1927.

Janowski Ł, Skarlatos D, Agrafiotis P et al. 2024. High resolution optical and acoustic remote sensing datasets of the Puck Lagoon. *Scientific Data*, **11**(1): 360, https://doi.org/10.1038/s41597-024-03199-y.

Li Z X, Peng Z T, Zhang Z et al. 2023. Exploring modern bathymetry: a comprehensive review of data acquisition devices, model accuracy, and interpolation techniques for enhanced underwater mapping. *Frontiers in Marine Science*, **10**: 1178845, https://doi.org/10.3389/fmars.2023.1178845.

Mohammadloo T H, Snellen M, Renoud W et al. 2019. Correcting multibeam echosounder bathymetric measurements for errors induced by inaccurate water column sound speeds. *IEEE Access*, **7**: 122052-122068, https://doi.org/10.1109/ACCESS.2019.2936170.

Mohammadloo T H, Snellen M, Simons D G. 2020. Assessing the performance of the multi-beam echo-sounder bathymetric uncertainty prediction model. *Applied Sciences*, **10**(13): 4671, https://doi.org/10.3390/app10134671.

Norgren P, Skjetne R. 2018. A multibeam-based SLAM algorithm for iceberg mapping using AUVs. *IEEE Access*, **6**: 26318-26337, https://doi.org/10.1109/ACCESS.2018.2830819.

Ogor J. 2018. Design of Algorithms for the Automatic Characterization of Marine Dune Morphology and Dynamics. Ocean, Atmosphere. ENSTA-Bretagne, Brest, France.

Palomer A, Ridao P, Ribas D. 2016. Multibeam 3D underwater SLAM with probabilistic registration. *Sensors*, **16**(4): 560, https://doi.org/10.3390/s16040560.

R2Sonic LLC. 2022. Sonic 2026/2024/2022 Operation Manual. R2Sonic LLC, USA.

Ruan X G, Cheng L, Chu S S et al. 2020. A new digital bathymetric model of the South China Sea based on the subregional fusion of seven global seafloor topography products. *Geomorphology*, **370**: 107403, https://doi.org/10.1016/j.geomorph.2020.107403.

Sotelo-Torres F, Alvarez L V, Roberts R C. 2023. An unmanned surface vehicle (USV): development of an autonomous boat with a sensor integration system for bathymetric surveys. *Sensors*, **23**(9): 4420, https://doi.org/10.3390/s23094420.

Xin M Z, Yang F L, Yan X P et al. 2015. An equivalent sound velocity profile iterative algorithm. *Hydrographic Surveying and Charting*, **35**(5): 28-31, 42, https://doi.org/10.3969/j.issn.1671-3044.2015.05.007. (in Chinese with English abstract)

Yang F L, Xu F Z, Fan M et al. 2022. An intelligent detection method for different types of outliers in multibeam bathymetric point cloud. *IEEE Transactions on Geoscience and Remote Sensing*, **60**: 5920710, https://doi.org/10.1109/TGRS.2022.3209344.

Yang F L, Xu F Z, Zhang K et al. 2020. Characterisation of terrain variations of an underwater ancient town in Qiandao Lake. *Remote Sensing*, **12**(2): 268, https://doi.org/10.3390/rs12020268.

Yu Y, Sandwell D T, Dibarboure G. 2024. Abyssal marine tectonics from the SWOT mission. *Science*, **386**(6727): 1251-1256, https://doi.org/10.1126/science.ads4472.